JGR Oceans

RESEARCH ARTICLE
10.1029/2022JC019275

Key Points:
- The simulated hydrographic structures over the Bellingshausen Sea continental shelf region are in good agreement with observations
- The warm water intrusions toward the Venable Ice Shelf show peaks of higher velocities in summer, likely caused by coastal trapped waves
- Glacial meltwater from about 33% of the area underneath the BS ice shelves flows into the Amundsen Sea within 2 years

Supporting Information:
Supporting Information may be found in the online version of this article.

Correspondence to:
S. Hyogo,
shuntaro1022@ees.hokudai.ac.jp

Citation:
Hyogo, S., Nakayama, Y., & Mensah, V. (2024). Modeling ocean circulation and ice shelf melt in the Bellingshausen Sea. *Journal of Geophysical Research: Oceans*, *129*, e2022JC019275. https://doi.org/10.1029/2022JC019275

Received 8 SEP 2022
Accepted 15 FEB 2024

Author Contributions:
Conceptualization: Shuntaro Hyogo, Yoshihiro Nakayama
Data curation: Shuntaro Hyogo, Yoshihiro Nakayama, Vigan Mensah
Formal analysis: Shuntaro Hyogo
Funding acquisition: Yoshihiro Nakayama
Methodology: Shuntaro Hyogo, Yoshihiro Nakayama, Vigan Mensah
Project administration: Yoshihiro Nakayama
Software: Shuntaro Hyogo, Yoshihiro Nakayama
Supervision: Yoshihiro Nakayama
Validation: Shuntaro Hyogo, Yoshihiro Nakayama
Visualization: Shuntaro Hyogo
Writing – original draft: Shuntaro Hyogo
Writing – review & editing: Shuntaro Hyogo, Yoshihiro Nakayama, Vigan Mensah

Modeling Ocean Circulation and Ice Shelf Melt in the Bellingshausen Sea

Shuntaro Hyogo[1], **Yoshihiro Nakayama**[2], **and Vigan Mensah**[2]

[1]Graduate School of Environmental Science, Hokkaido University, Sapporo, Japan, [2]Institute of Low Temperature Science, Hokkaido University, Sapporo, Japan

Abstract The ice shelves in the Bellingshausen Sea are melting and thinning rapidly due to modified Circumpolar Deep Water (mCDW) intrusions carrying heat toward ice-shelf cavities. Observations are, however, sparse in time and space, and extensive model-data comparisons have never been possible. Here, using a circulation model of the region and ship-based observations, we show that the simulated water mass distributions in several troughs traversing mCDW inflows are in good agreement with observations, implying that our model has the skills to simulate hydrographic structures as well as on-shelf ocean circulations. It takes 7.9 and 11.7 months for mCDW to travel to the George VI Ice Shelf cavities through the Belgica and Marguerite troughs, respectively. Ice-shelf melting is mainly caused by mCDW intrusions along the Belgica and Marguerite troughs, with the heat transport through the former being ~2.8 times larger than that through the latter. The mCDW intrusions toward the George VI Ice Shelf show little seasonal variability, while those toward the Venable Ice Shelf show seasonal variability, with higher velocities in summer likely caused by coastal trapped waves. We also conduct particle experiments tracking glacial meltwater. After 2 years of model integration, ~33% of the released particles are located in the Amundsen Sea, supporting a linkage between Bellingshausen Sea ice-shelf meltwater and Amundsen Sea upper ocean hydrography.

Plain Language Summary The Bellingshausen Sea Ice Shelves have been affected by high ice-shelf melt and ice-loss rates in Antarctica. The reason for the ice loss is the presence of warm modified Circumpolar Deep Water (mCDW) over the continental shelf, which intrudes into ice-shelf cavities. Recently, studies combining observations and models have significantly advanced our understanding of Ice-Ocean interactions around Antarctica. For example, in the Amundsen Sea, the region neighboring the Bellingshausen Sea and contributing the most to Antarctic glacial ice loss, such an approach has revealed the drivers and pathways of ocean heat intrusions as well as the impact of glacial meltwater on the Antarctic coastal circulation. We follow this approach and evaluate our ocean model by comparing it with ship-based and satellite-based observations. Using this model simulation, we show that the simulated mCDW intrudes from the continental shelf break toward ice-shelf cavities mainly through two deep cross-shelf troughs. The glacial meltwater is transported by the westward Antarctic Coastal Current (AACC) flowing into the Amundsen Sea. The mCDW inflow and AACC in the coastal area show seasonal variabilities with higher velocities in the summer, which are likely caused by coastal trapped waves.

1. Introduction

The ice shelves and glaciers of the West Antarctic Ice Sheet (WAIS) have experienced thinning (Paolo et al., 2015), melting (Adusumilli et al., 2020; Pritchard et al., 2012; Rignot et al., 2013, 2019), and mass loss (Cook et al., 2016; B. Smith et al., 2020; Wouters et al., 2015), contributing to rising global sea levels and changes in the state of the Southern Ocean (Bamber et al., 2009; S. Jacobs et al., 2002; Nakayama et al., 2020; Rintoul, 2007). High basal melting of the ice shelves in the Amundsen Sea (AS) and the Bellingshausen Sea (BS) are caused by intrusions of warm water referred to as modified Circumpolar Deep Water (mCDW, about 0.5–1.5°C located below 300–500 m (Nakayama et al., 2017)) through deep cross-shelf troughs (Jenkins & Jacobs, 2008; D. Martinson & McKee, 2012; Wåhlin et al., 2013; X. Zhang et al., 2016). When this warm mCDW meets the ice shelf, it forms a buoyant mixture of mCDW and glacial meltwater (Dutrieux et al., 2014; S. S. Jacobs et al., 1996; Nakayama et al., 2018). This mixture is mainly transported by the Antarctic Coastal Current (AACC) westward along the Antarctic coast (Dinniman et al., 2016; Kusahara & Hasumi, 2014; Nakayama et al., 2013, 2014, 2020). Quantitative understanding of these processes is crucial for predicting future changes in the Antarctic mass budget and global sea levels.

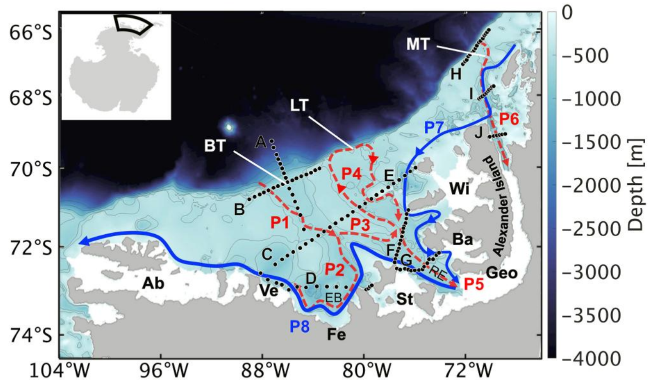

Figure 1. Map of model bathymetry (color). Bathymetric contours of 500, 600, 1,000, 1,500, and 2,000 m are shown in black. The inset (left top) shows Antarctica, with the region surrounded by a black line denoting the model domain. The black (A–J) dots represent vertical sections in the Belgica, Latady, and Marguerite troughs. Locations of hydrographic profiles collected from cruise JR-165 (black dots) are shown. The locations of ice shelves are shown with white patches, George VI Ice Shelf (Geo), Wilkins Ice Shelf (Wi), Bach Ice Shelf (Ba), Stange Ice Shelf (St), Venable Ice Shelf (Ve), and Abbot Ice Shelf (Ab). Other features include Belgica Trough (BT), Latady Trough (LT), Marguerite Trough (MT), Eltanin Basin (EB), and Ronne Entrance (RE). The circulation's schematic is represented by the red (modified Circumpolar Deep Water) and blue (Antarctica Coastal Current) arrows, which is inferred from simulated velocity and particle experiments.

In the BS, warm mCDW accesses the ice-shelf cavities through the Marguerite, Latady, and Belgica troughs (Figure 1). The Marguerite Trough has been relatively well investigated and hydrographic data show that mCDW intrudes through the submarine glacial trough to the northern George VI Ice Shelf (Dinniman & Klinck, 2004; Dinniman et al., 2011; Graham et al., 2016; Jenkins & Jacobs, 2008; D. G. Martinson et al., 2008; D. A. Smith et al., 1999; St-Laurent et al., 2013; C. Walker & Gardner, 2017). Moffat et al. (2008) and D. Martinson and McKee (2012) suggest that on-shelf mCDW transfer is governed by eddies shedding from the Antarctic Circumpolar Current along the shelf break at the mouth of Marguerite Trough. Glacial meltwater from the George VI Ice Shelf flows westward, carried by the AACC. The AACC variability is considered to be linked to both wind and buoyancy forcing (Holland et al., 2010; T.-W. Kim et al., 2017; Moffat et al., 2008).

In the Latady Trough, the presence of mCDW was first identified by Talbot (1988) using hydrographic data. Some observational studies suggest that mCDW travels along the eastern boundary of the Latady Trough toward the Wilkins, Bach, and South George VI ice shelves and then return to the shelf break along the western flank of the trough (Ruan et al., 2021; Schulze Chretien et al., 2021; Thompson et al., 2020). However, no direct observations support cross-slope mCDW exchange through the Latady Trough, so the origin of the water flowing into this Trough remains unclear (Schulze Chretien et al., 2021). Previous modeling studies of the BS do not show cross-slope mCDW intrusions toward the Latady Trough (Graham et al., 2016; Nakayama et al., 2017).

Along the eastern boundary of the Belgica Trough, mCDW travels toward the Ferrigno and Venable ice shelves (Schulze Chretien et al., 2021; Thompson et al., 2020; X. Zhang et al., 2016). Using ocean models, Graham et al. (2016) and Nakayama et al. (2017) suggest that mCDW reaches the southern coast near the Eltanin Basin within 90 days via the Belgica Trough. The simulated mCDW intrusions onto the Belgica Trough show two pathways toward the Venable and the Latady Trough directions. The Venable Ice Shelf is smaller than other BS ice shelves but has been estimated to have a large area average basal melt rate (Paolo et al., 2015; Rignot et al., 2013). Consequently, meltwater is found to be elevated at the western edge of the Belgica Trough (Ruan et al., 2021; X. Zhang et al., 2016).

The linkage between the AS and BS has been pointed out by several studies (Dawson et al., 2023; Flexas et al., 2022; Nakayama et al., 2014; Ruan et al., 2021; Schubert et al., 2021; Schulze Chretien et al., 2021). Nakayama et al. (2014) and Regan et al. (2018), for example, simulated the spreading of glacial meltwater from BS ice shelves. Ruan et al. (2021) and Schubert et al. (2021) investigated the role of the Antarctic coastal current and how effectively it carries glacial meltwater using observations. Sheehan et al. (2023) investigate the distribution of glacial meltwater using observations traversing the Belgica trough and suggest that they can identify different origins based on their hydrographic properties and turbidity. However, none of these studies, quantitatively investigated how much glacial meltwater flows from the BS ice shelves into the AS and how long it takes to get there. Additionally, Flexas et al. (2022) proposes a similar mechanism that ice shelf meltwater injection in the Antarctic Peninsula region can promote ice shelf melting across West Antarctica by conducting a high-resolution numerical model.

The limited observations on the BS continental shelf made it difficult to compare model output with observations to evaluate the spatial water mass structures. Here, we evaluate the ocean model extensively in the BS by comparing it with observations, including ship-based and seal Conductivity-Temperature-Depth (CTD) observations and ice shelf/sea ice data from satellites, including newly recognized ship-based observations. These ship-based observations are more than 15 years old, but the polar community started to recognize these observations only recently. The first oceanography paper describing these observations was only published in 2020 (Ruan et al., 2021; Thompson et al., 2020). In this paper, we present the simulated ocean circulation and how mCDW and glacial melt water circulates over the BS continental shelf, including the linkage between the BS and AS. We also investigate the mechanism of the simulated seasonal variabilities of mCDW intrusions and AACC strength.

2. Methods

2.1. Model Settings

Following Nakayama et al. (2018), we conduct a regional ocean simulation using a regional AS and BS configuration of the Massachusetts Institute of Technology general circulation model (MITgcm) (Marshall, Adcroft, et al., 1997; Marshall, Hill, et al., 1997), which includes dynamic/thermodynamic sea ice (Losch et al., 2010) and thermodynamic ice-shelf (Losch, 2008) capabilities. We also extend the calculation period from 1992 to 2017 and validate the reproducibility of the model for observations in the BS. The model domain contains the AS and BS (black line in Figure 1 inset). The model uses a latitude–longitude grid north of 70°S and a bipolar grid south of 70°S (see Forget et al. (2015) for details) with a horizontal grid spacing in the BS of 2–4 km. The horizontal resolution is not fully eddy resolving over the continental shelf (Graham et al., 2016; Nakayama et al., 2017). The vertical discretization comprises 70 levels varying in thickness from 10 m near the surface, 70–90 m at depths of 500–1,000 m, and 450 m at the deepest level of 6,000 m. The model bathymetry is based on the International Bathymetric Chart of the Southern Ocean (IBCSO) (Arndt et al., 2013) and the model ice draft is based on Antarctic Bedrock Mapping (BEDMAP-2) (Fretwell et al., 2013). The initial conditions are derived from a 16 years (2001–2016) spin-up, integrated from rest and from January World Ocean Atlas 2009 temperature (Locarnini et al., 2010) and salinity (Antonov et al., 2010) fields. Surface forcing for the 1992–2017 period is provided by ECCO (Estimating the Circulation and Climate of the Ocean) LLC270 (H. Zhang et al., 2018), which is based on ERA-Interim (Dee et al., 2011) and has been adjusted using the ECCO adjoint model-based methodology (Wunsch & Heimbach, 2013). Lateral boundary conditions for ocean and sea ice states in 1992–2017 are provided by the ongoing ECCO LLC270 optimization. This model does not account for tidal forcing. The changes from Nakayama et al., 2018 in this model are (a) updating the model calculation period to 26 years, 1992–2017, (b) changing model parameters (Tables S1 and S3 in Supporting Information S1), and (c) comparing the model with observations in the BS, which had been previously included in this model domain, but had yet to be analyzed in detail. To adjust the melt rate of the George VI Ice Shelf with reference to Rignot et al. (2013), we change the values of the heat transfer coefficient (γ_T) from 0.5×10^{-4} m s^{-1} to 0.25×10^{-4} m s^{-1}, similar to Nakayama et al. (2018) (Table S3 in Supporting Information S1). Particle release experiments are conducted to analyze the circulation patterns of mCDW intrusions and glacial meltwater using Octopus (https://github.com/jinbow/Octopus).

2.2. Hydrographic Observations

We evaluate our model in the Belgica, Latady, and Marguerite troughs by comparing simulated results with ship-based data and biologging observations. The CTD and Argo data are from the World Ocean Database 2018 (Boyer et al., 2018). We primarily use the CTD data in each trough collected by the R/V James Clark Ross (cruise JR165) between 3 March and 9 April 2007 (Castro-Morales et al., 2013). The biologging data are obtained from the Marine Mammals Exploring the Oceans Pole to Pole consortium (Treasure et al., 2017). These data have estimated uncertainties of ±0.02°C for temperature and ±0.02 for salinity (Roquet et al., 2011). We use seals data only for March from 2001 to 2017.

2.3. Heat Transport Calculation

We calculate temperature transports through various sections relative to the in situ freezing point of seawater following Kalén et al. (2016) and B. G. Webber et al. (2019). For a given section, the total heat transport is given by

$$Q_H = \int_{x1}^{x2} \int_{-H}^{0} \rho C_p v \left(T - T_f\right) \mathrm{d}x\, \mathrm{d}z \tag{1}$$

where x is the horizontal distance (m), x_1 and x_2 define the horizontal limits of the section, z is height and H is the local depth of the deepest model level (m), ρ is the in situ density (kg m^{-3}), C_p is the specific heat capacity of seawater (J kg^{-1} K^{-1}), v is the velocity component normal to the section in the onshore direction (m s^{-1}), T is the potential temperature (°C), and T_f is the surface freezing point temperature. Q_H represents the heat available to melt ice (e.g., D. P. Walker et al. (2007)). We refer to this quantity as heat transport, even though it is not strictly

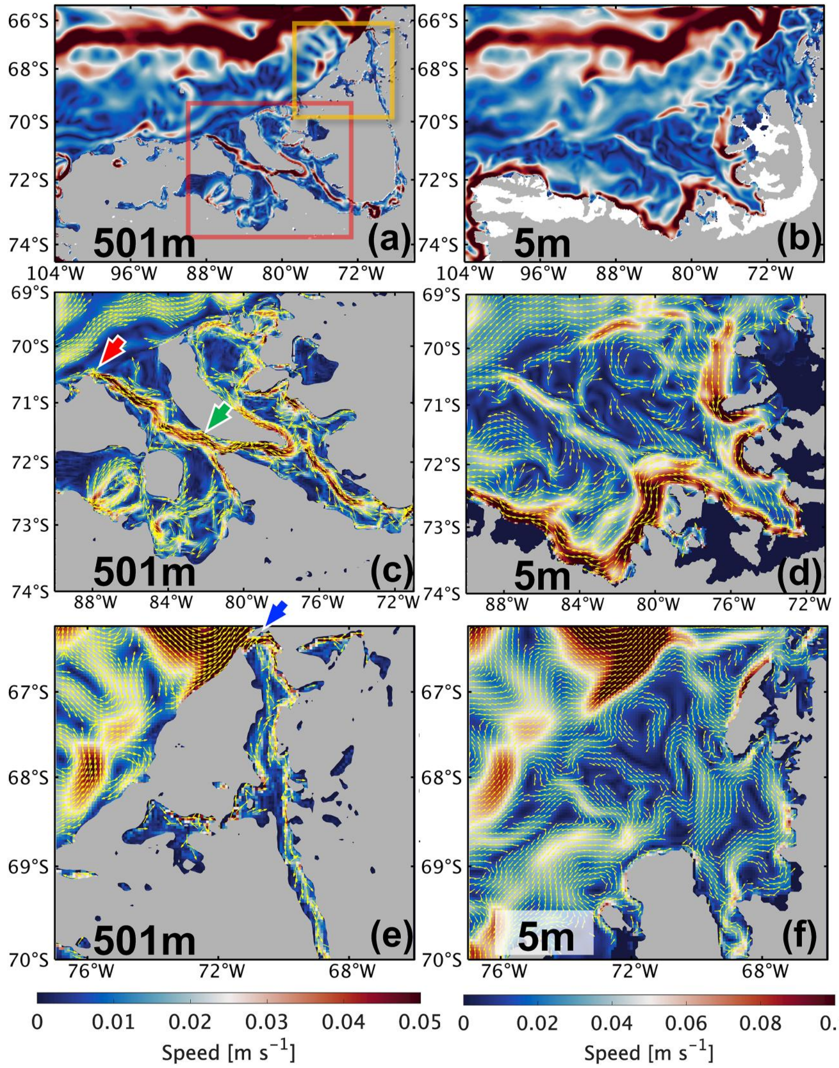

Figure 2. Simulated speed of the time mean velocities (1992–2017) at 501 m in the (a) Bellingshausen Sea, (c) Belgica and Latady troughs (the red box in a), and (e) Marguerite trough (the yellow box in a). Yellow arrows indicate direction of the time mean velocities (c–f). Because of limited space in the figure, only 25% of the yellow arrows (direction) are plotted. (b, d, f) Same as the left figures but for a depth of 5 m.

appropriate to determine a heat transport (or heat flux) through a section with nonzero volume flux (e.g., Schauer and Beszczynska-Möller (2009)).

3. Results

3.1. Simulated Ocean Circulation Over the BS Continental Shelf

Figure 2 represents the average circulation over the entire simulation period from 1992 to 2017. Cross-shelf mCDW transport into the Belgica Trough occurs from the western side of the Trough (Figure 2a, red arrow in Figure 2c; see pathway P1 in Figure 1), as discussed in more detail in Sections 3.3. The mCDW travels about 200 km from 71°S to 72°S (pathway P1 in Figure 1) and then separates into 2 pathways (green arrow in Figure 2c; pathways P2 and P3 in Figure 1). The first pathway toward the Eltanin Basin (see pathway P2 in Figure 1) follows a clockwise circulation toward the Venable Ice Shelf, which is consistent with previous studies (Graham et al., 2016; Holland et al., 2010; Nakayama et al., 2017; X. Zhang et al., 2016). The other mCDW pathway, toward the Latady Trough, separates into two pathways (pathways P3, P4, and P5 in Figure 1): the first extends toward the direction of the shelf break along the western flank of the Latady Trough and returns following the

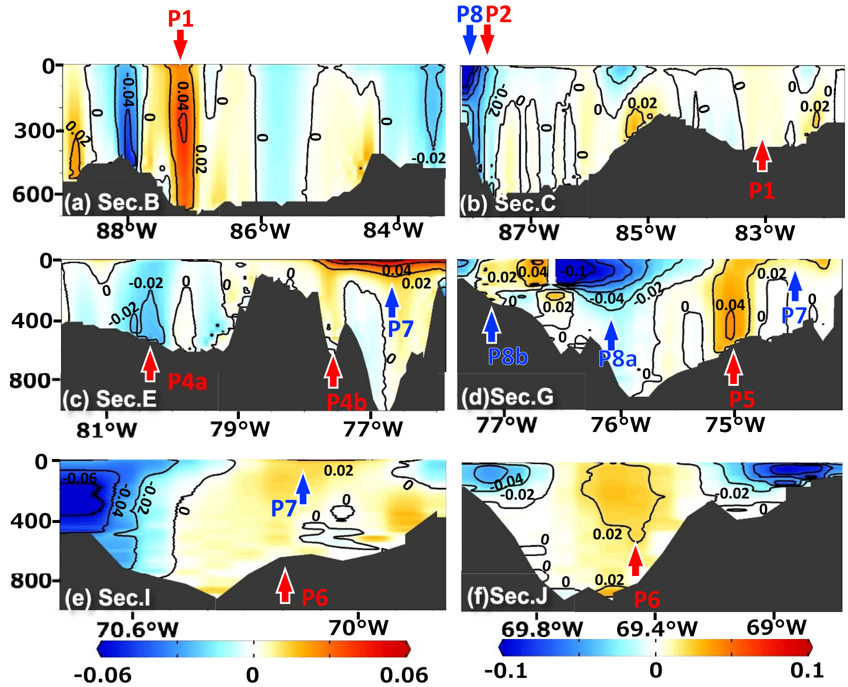

Figure 3. Vertical sections of simulated southward time mean velocities (1992–2017) in cross sections (a) B, (b) C, (c) E, (d) G, (e) I, and (f) J. The black contour interval is 0.02 m s^{-1}. The red and blue arrows indicate the mCDW and AACC, respectively, with each label corresponding to Figure 1. The same arrows in Figure 1 appears more than once in a section; it is distinguished by alphabetical characters.

eastern flank of the trough (Figure 2c; see pathway P4 in Figure 1), while the second goes toward the Ronne Entrance and intrudes into the George VI ice-shelf cavity (Figure 2c; see pathway P5 in Figure 1). Our simulation yields no cross-shelf mCDW transport through the Latady Trough (Figure 2c), consistent with the results of mCDW tracer experiments in previous studies (e.g., Graham et al., 2016; Nakayama et al., 2017). Observations show that the coldest mCDW is found at the shelf break at the westernmost edge of the Latady Trough, but the origin of the water flowing into this trough remains unclear (Schulze Chretien et al., 2021).

Cross-shelf mCDW transport into the Marguerite Trough occurs from the shelf break at ~66.5°S (Figure 2a, blue arrow in Figure 2e; see P6 red pathway in Figure 1). The mCDW intrudes from the continental shelf break through the Marguerite Trough toward the northern George VI Ice Shelf.

Cross-sections B and C (Figures 3a and 3b, see Figure 1 for cross-section locations) highlight the barotropic structures of mCDW intrusions through the Belgica Trough. The strong southward current (~0.04 m s^{-1}) at 87–87.5°W in cross-section B represents the mCDW intrusion (red pathway P1 in Figure 3a), which is linked with the southward flow at 83°W in cross-section C (red pathway P1 in Figure 3b). In the Latady Trough, cross-sections E and G (Figures 3c and 3d, see Figure 1 for cross-section locations) exhibit northward and southward currents. The northward current at 80–81°W in cross-section E indicates the mCDW intruding from the Belgica Trough (see Figure 2c, red pathway P4a in Figure 3c), whereas the southward currents indicate the mCDW intrusions returned from the Latady shelf break (red pathway P4b in cross-section E). In Figure 3d, the southward flow with a barotropic structure indicates mCDW intrusion toward the southern George VI Ice Shelf (red pathway P5 in Figure 3d). For the Marguerite Trough, cross-sections I and J show a southward current of ~0.01–0.02 m s^{-1} (red pathways P6 in Figures 3e and 3f).

The AACC flows toward the northern side of Alexander Island along the edge of the Wilkins Ice Shelf (Figure 2f), which is consistent with earlier studies (Moffat et al., 2008; Schubert et al., 2021). We also refer to the AACC, which is the strong westward flowing coastal current near the Belgica and Latady troughs (Figures 2b and 2d; blue pathways P7 and P8 in Figure 1). The AACC flows to the AS through the Belgica Trough and along the Venable and Abbot ice-shelf fronts (see Figuress 2b and 2d). In the Marguerite Trough, the AACC flows southward from the Antarctic peninsula at 0.02 m s^{-1} at the surface (blue pathway P7 in Figure 3e). The AACC between the

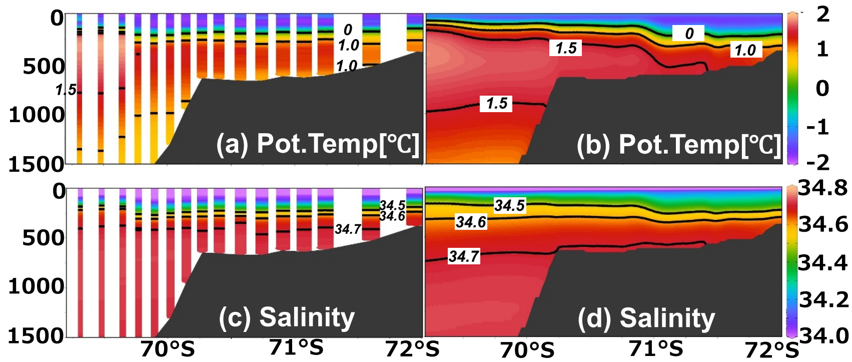

Figure 4. Observed vertical sections of (a) potential temperature and (c) salinity in March 2007 along section A (Figure 1) collected by the R/V James Clark Ross (cruise JR165). Simulated vertical sections of monthly mean (b) potential temperature and (d) salinity in March 2007 along the same section. For salinity, contours of 34.5, 34.6, and 34.7 are shown in black. For potential temperature, contours of 0, 0.5, 1.0, and 1.5° are shown in black.

northern side of Alexander Island and the Ronne Entrance has southward currents with a maximum velocity of ~0.1 m s^{-1} above depths of 200 m (blue pathways P7, P8a, and P8b in Figures 3c and 3d). Especially in the Belgica Trough, the AACC flows in the same direction as the mCDW intrusions (see Figures 2c and 2d, and pathways P2 and P8 in Figure 3b).

3.2. Model Evaluation

For the Belgica, Latady, and Marguerite troughs, the model shows cold and fresh Winter Water (WW, about 1.5°C and salinity <34.4 (Dutrieux et al., 2014)) in the upper layer and mCDW in the lower layer (Figures 4–7, see Figure 1 for the locations of cross-sections A–J). For cross-slope Section A, both the model and observations show mCDW in the Belgica Trough at depths below 200 m (Figure 4). Water mass distributions below depths of 500 m over the continental shelf exhibit almost similar properties.

For cross-trough sections B and C, the cores with the simulated and observed maximum potential temperature are in the Belgica shelf break of section B (between 84 and 87.5°W in Figures 5a and 5b) and the eastern side of section C (between 82 and 84°W in Figures 5c and 5d), corresponding to the red pathway P1 in Figure 1. The simulated mCDW potential temperatures for sections B, C, and D (defined as the maximum potential temperatures below a depth of 200 m) are 1.61, 1.57, and 1.42°C, which are slightly warmer than the observed values (1.44, 1.44, and 1.28°C, respectively; see Figure 5 and Table S2 in Supporting Information S1). The change in maximum potential temperature from the continental shelf break toward the Antarctic coast along the Belgica Trough is small in both the model and observations, but observed and simulated mean 1.0°C isotherms deepen toward the coast. The mean simulated 1.0°C isotherm depths of sections B, C, and D are 232 ± 58, 348 ± 60, and 357 ± 35 m, while the observed thermocline depths are 285 ± 37, 292 ± 42, and 397 ± 73 m, respectively (Figure 5 and Table S2 in Supporting Information S1). The simulated 1.5°C potential temperature and 34.5 salinity contours at the shelf break have a steep gradient at ~87.5°W, which indicates that mCDW intrusion occurs from the west side of the Belgica Trough (the red pathways in Figures 5a and 5b). The mCDW intrudes toward the eastern side from the western side across the Belgica Trough (Figure 2a). Previous observational studies show mCDW intruding onto the continental shelf from the eastern side of the Belgica Trough (Ruan et al., 2021; Schulze Chretien et al., 2021; Thompson et al., 2020; X. Zhang et al., 2016). In our simulation, mCDW enters from the west side, which may be caused by missing bathymetric features in the model bathymetry.

For cross-trough sections E, F, and G in the Latady Trough, the latitudinal change of potential temperature in the WW and mCDW are small in both the model and data, but observed and simulated mean 1.0°C isotherm depths become deeper toward the coast (Figure 6 and Table S2 in Supporting Information S1). The simulated thermocline depths for sections E, F, and G are 276 ± 19, 294 ± 28, and 320 ± 26 m, while the observed thermocline depths are 298 ± 55, 322 ± 38, and 371 ± 47 m, respectively (Figure 6 and Table S2 in Supporting Information S1). For the cross-trough sections H, I, and J in the Marguerite Trough, the simulated mCDW flowed into the Marguerite Trough with warm water (Figure 7). For the eastern side of sections H and I, the peak of the simulated

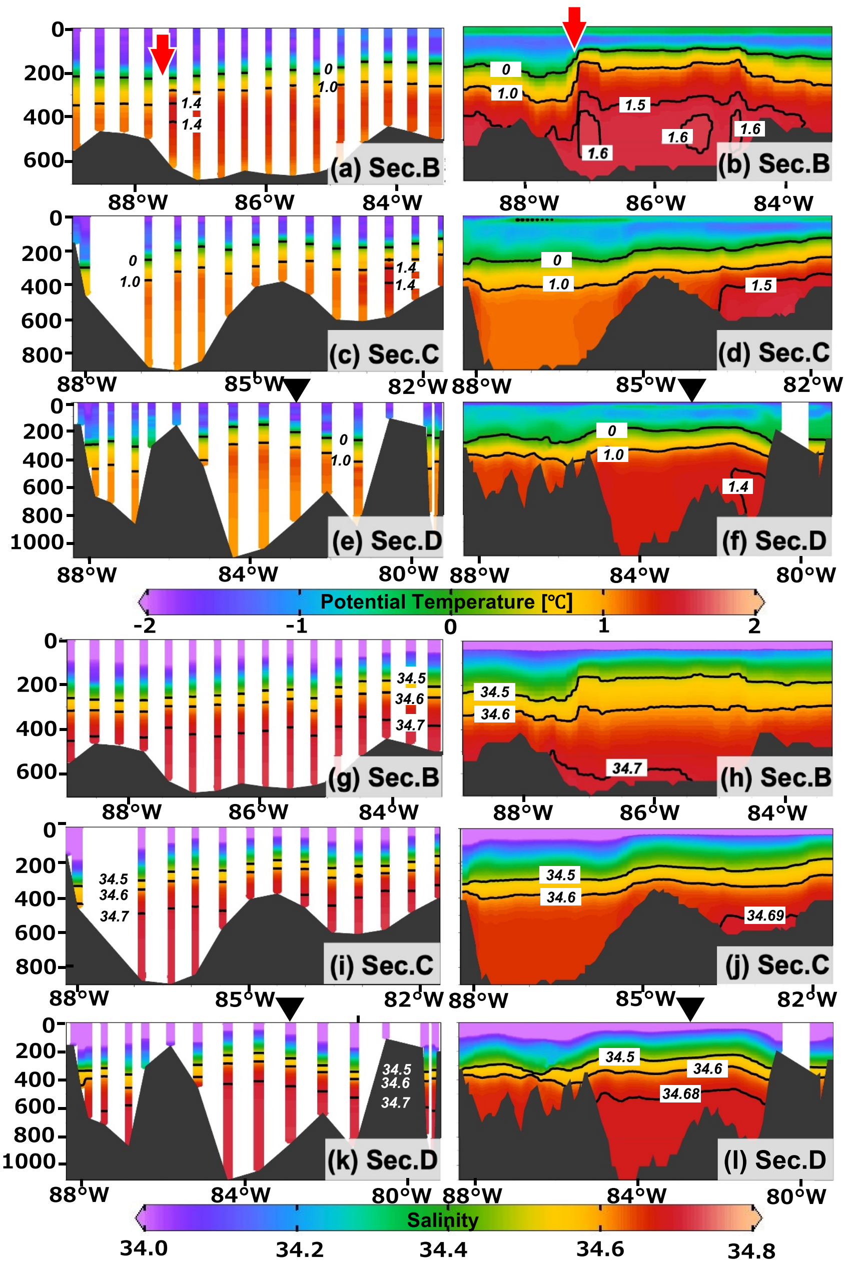

Figure 5. Same as in Figure 4 but for sections B, C, and D (see Figure 1 for the locations of each section). For potential temperature, contours of 1.4 and 1.6° are added. For salinity, contours of 34.68 and 34.69 are added. The black triangles indicate the locations of the CTD observations shown in Figure S1 in Supporting Information S1.

potential temperature (~1.5–1.7°C) can be found, which is consistent with observations (the blue pathway in Figures 7a and 7b). On the continental shelf break in the Marguerite Trough, the tilting of the simulated 1.5°C isothermal line is similar to observations between 70.5°W and 71°W (blue pathways in Figures 7a and 7b).

To verify the spatially simulated ocean profiles of the nearby thermocline and mCDW intrusions in the BS, we compare the model data with observations at depths of 215 and 501 m (Figure 8). The simulated March mean potential temperature and salinity from 1992 to 2017 at a depth of 501 m show good consistency with the observations (Figures 8a and 8c), however, the potential temperature of mCDW is warmer than observations by ~0.2°C, and its salinity is ~0.05 lower. The simulated March mean salinity and potential temperature from 1992 to 2017 at a depth of 215 m are in good agreement with the observation data, indicating that the horizontal

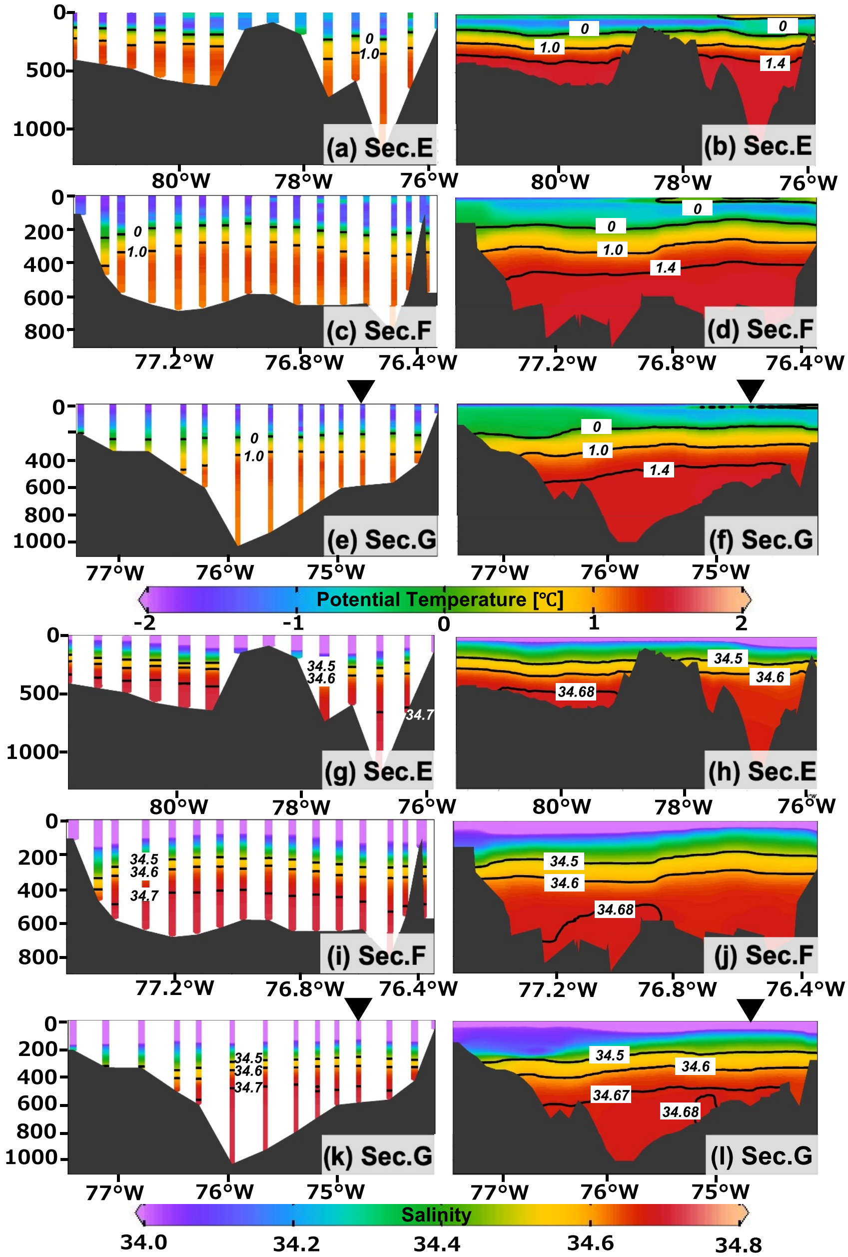

Figure 6. Same as in Figure 4 but for sections E, F, and G. For potential temperature, contour of 1.4° is added. For salinity, contours of 34.67 and 34.68 are added. The black triangles indicate the locations of the CTD observations shown in Figure S1 in Supporting Information S1.

distribution of WW properties agrees well with observations in most of the BS (Figures 8b and 8d). The model is capable of capturing the tilting of temperature and salinity from the western to eastern parts of the BS shelf. A small difference is observed in all parts, with the simulated temperature and salinity underestimated by ~0.5°C and ~0.1, respectively. This is caused by a mismatch of the thermocline depth in the model. One reason may be that the model does not incorporate iceberg melt related to WW thickness.

The simulated winter mean (September) sea ice extent is similar to satellite-based estimates (see Figures S2b and S2d in Supporting Information S1) (Comiso, 1986, 2017), while the simulated mean summer (March) sea ice extent on the continental shelf is underestimated by ~20% (Figures S2a, S2c, and S3 in Supporting Information S1).

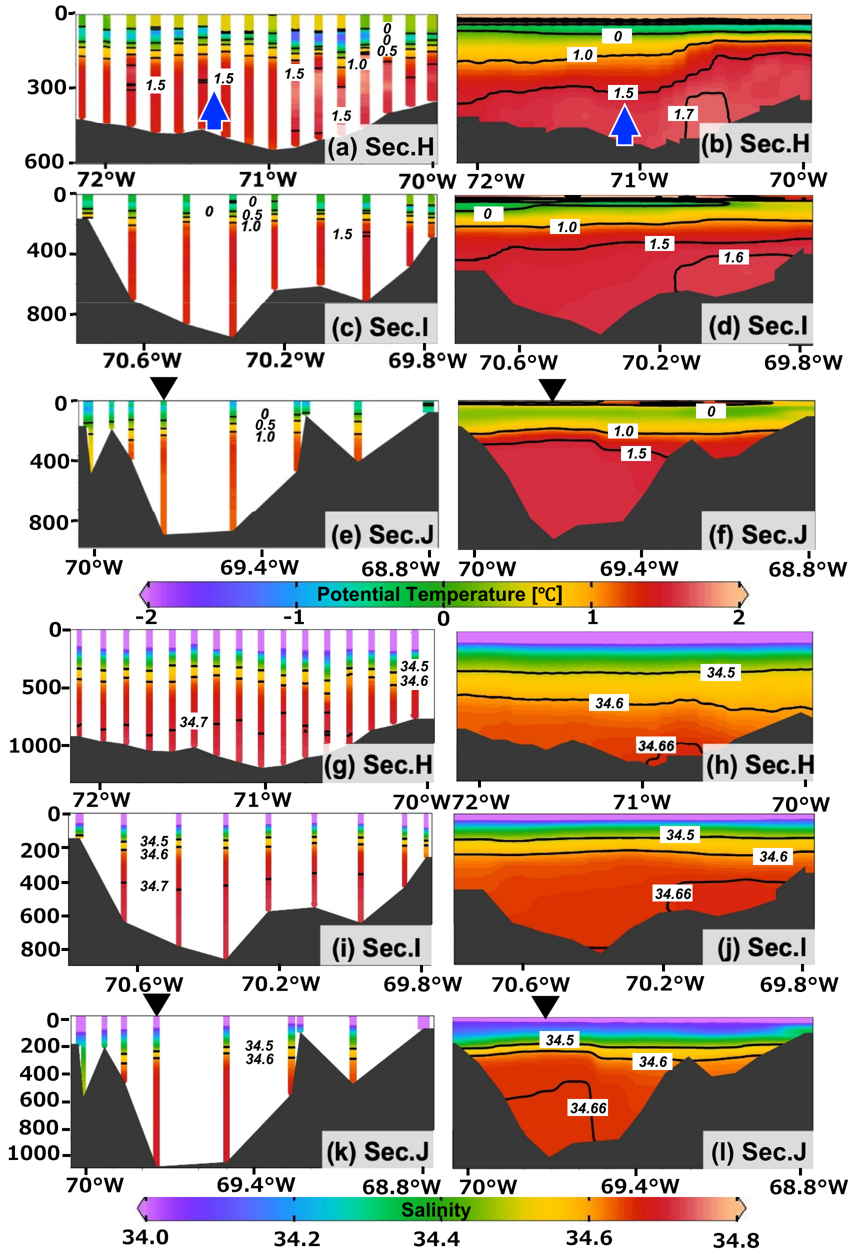

Figure 7. Same as in Figure 4 but for sections H, I, and J. For potential temperature, contous of 0.5, 1.6, and 1.7° are added. For salinity, contour of 34.66 is added. The black triangles indicate the locations of the CTD observations shown in Figure S1 in Supporting Information S1.

Simulated basal melt rates are compared with two observation-based estimates (Adusumilli et al., 2020; Rignot et al., 2013) (Table S3 in Supporting Information S1). In the GeorgeVI and Wilkins ice shelves, the simulated basal melt rate is overestimated compared to satellite observations. In the Stange and Venable ice shelves, the simulated basal melt rate is overestimated in 2010–2017, while the observed basal melt rate for 2003–2008 is almost identical. However, the ice-shelf melting in the Abbot Ice shelf is underestimated for both periods. Such differences may be caused by (a) the model bathymetry and the ice-shelf draft being different from reality or (b) simulated mCDW in ice shelf cavities warmer than reality.

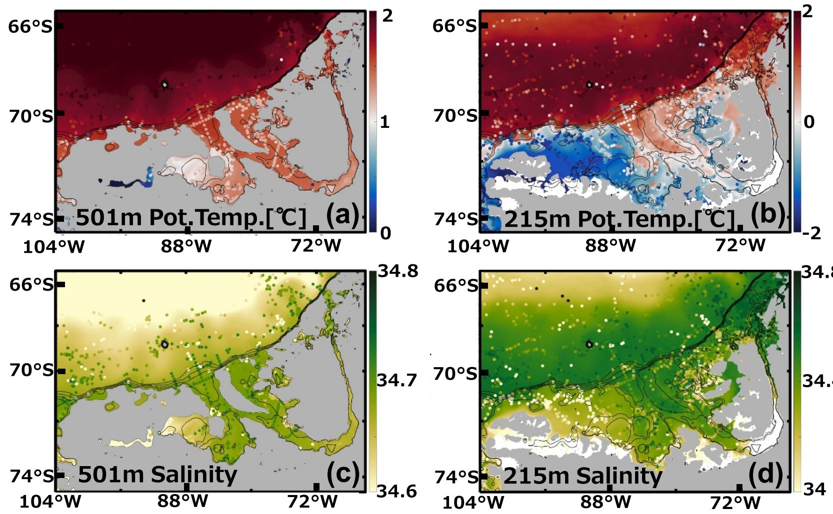

Figure 8. Simulated (a) potential temperature and (c) salinity at 501 m in March climatology between 1992 and 2017. The dots indicate the location of the CTD, Argos, and seal data which plots the closest values to a particular depth in the model, and only for March from 2001 to 2007. The color of the dots shows their (a) potential temperature and (c) salinity at a depth of 501 m. (b, d) Same as left figures but for a depth of 215 m.

3.3. Simulated mCDW Intrusions Toward the BS Ice Shelves

We conduct backward particle release experiments offline using time mean outputs of ocean velocity between 1992 and 2017. The particles are placed in the water mass under the BS ice shelves with a potential temperature of 0.5°C or higher to investigate the mCDW intrusions (see plots in Figure 9a). The mCDW pathways in the Belgica,

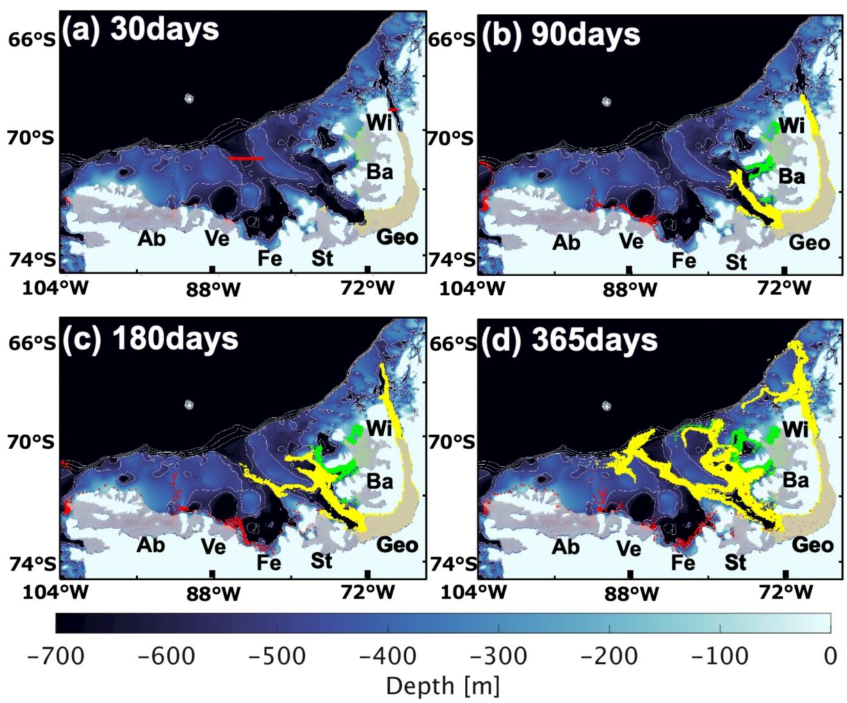

Figure 9. Spatial distributions of backtracking particles (yellow points) released under the Wilkins and Bach (green plot), George VI and Stange (yellow plot), and Venable and Abbot (red plot) ice shelves with potential temperatures higher than 0.5°C (a) 30, (b) 90, (c) 180, and (d) 365 days before the particles released using time mean daily velocity (1992–2017). The contours of depths of 500, 600, 1,000, 1,500, and 2000 m are shown in white. The locations of ice shelves are shown with gray patches. The red lines in (a) are used to derive the heat transport in Figure 10.

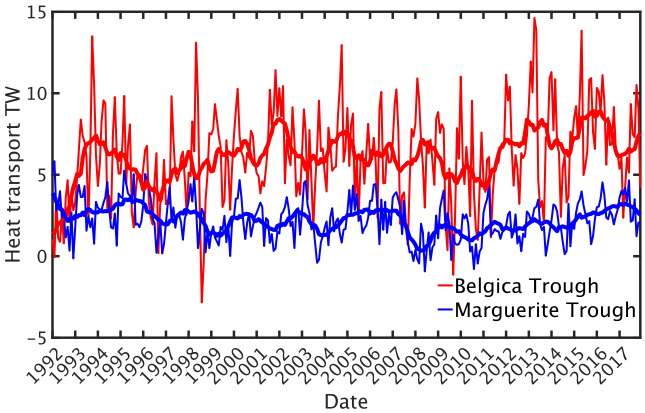

Figure 10. Monthly mean (thin lines) time series of heat transport (TW; positive toward south) through the Belgica (red) and Marguerite (blue) troughs. The bold lines indicate 12-month running means. See Figure 9a for section locations.

Latady, and Marguerite troughs follow the ∼500 m bathymetric contours, which is consistent with the time mean velocity (Figures 2c and 9d). After 90 days, the particles released from the southern George VI Ice Shelf are located at the center of the Latady Trough (∼72°S; see Figure 9b), and after 180 days, they are found in the Belgica Trough (∼71°S; see Figure 9c). Lastly, the particles released from the southern George VI Ice Shelf are located on the shelf break of the Belgica Trough after 365 days of spreading in the east-west direction. The particles released from the northern George VI Ice Shelf are located at the shelf break in the Marguerite Trough within 365 days. Similar experiments conducted for each year starting on December 31 from 1992 to 2017 using daily mean outputs of ocean velocity show similar pathways (Figure S4 in Supporting Information S1). We find that it takes 7.9 ± 1.8 months (mean ± 1 SD) for particles in the Belgica Trough to reach the southern George VI Ice Shelf, and 11.7 ± 4.7 months for the mCDW in the Marguerite Trough to reach the northern George VI Ice Shelf (Table S4 in Supporting Information S1).

Particles placed on the Bach and Wilkins ice shelves are located in the Latady Trough after 365 days (see green plots in Figure 9d), with the particles from the Wilkins Ice-shelf outflowing from two ice fronts. Particles from the Venable Ice Shelf are located under southern George VI after 365 days. Particles from the Abbot Ice Shelf show two intrusions from the AS shelf break after about 90 days, and from near the Eltanin Basin in 365 days.

The time mean heat transport is 6.2 ± 2.8 TW and 2.2 ± 1.3 TW for the Belgica and Marguerite troughs, respectively (Figure 10; see Figure 9a for section locations). At the interannual time scale, the heat transport in the Belgica Trough increases between 1992 and 1994, stays at ∼5.9 ± 2.6 TW between 1994 and 2010, and increases until 2017 (bold red line in Figure 10). Heat transport is large in 1993, 1998, 2004, 2013, and 2015, and is small (negative) in 1998 and 2009. The heat transport in the Marguerite Trough is nearly stable at the interannual scale, at ∼2.2 ± 1.3 TW throughout the simulation period (bold blue line in Figure 10). At the mid-shelf section in the Belgica Trough, the southward heat transport is estimated to be a net value of 370 ± 280 GW for 2019 using oceanographic observations (Schulze Chretien et al., 2021). Our simulated transport (6.2 ± 2.8 TW) and the simulated transport of Graham et al. (2016) (maximum of ∼5.0 TW) are much larger than the observational estimates. It is possible that observations are conducted during weak mCDW inflow, considering that observations are conducted only for 2 weeks and simulated heat transports present large variabilities in seasonal to interannual time scales (Figure 10).

3.4. Spreading of Glacial Meltwater From BS Ice Shelves

The forward particles release experiments are conducted offline using time mean data created by outputs of ocean velocity between 1992 and 2017. We also conducted a 2-year forward particle tracking experiment using daily mean outputs of ocean velocity each year between 1992 and 2017 and investigated the impact of each BS ice-shelf melting toward the AS. The particles are placed in the top ocean model layer underneath any grid cell where the time mean net ice shelf basal melt (1992–2017) is downward to investigate the spreading of the glacial meltwater. The particles from the Wilkins and Bach ice shelves outflow from the western side of the ice front after 30 days. These particles flow along the coast and are located on the southern George VI, Stange, Ferrigno, Venable, and Abbot ice shelves after 365 days (Figures 11a and 11b). The George VI and Stange ice-shelf particles follow two pathways from the northern George VI Ice Shelf and the Ronne entrance after 30 days (Figure 11c). After 365 days, the particles from the southern George VI and Stange ice shelves flow westward along the coast and reach the AS (near 103°W) (Figure 11d). In addition, the particles from the northern George VI Ice Shelf flow through Marguerite Bay toward the north side of Alexander Island and toward the Antarctic Peninsula (Figure 11d). The particles from the Abbot and Venable ice shelves show some outflow to the AS after 30 days, and after 365 days, they flow toward the south along the coast (Figures 11e and 11f). These particle pathways are in good agreement with the results of tracer experiments obtained by Sheehan et al. (2023).

For the particles discharged from each Ice Shelf, it takes 153 ± 46 days, 102 ± 35 days, 384 ± 93 days, and 232 ± 58 days to reach the AS from the Venable Ice Shelf, southern George VI and Stange ice shelves, northern

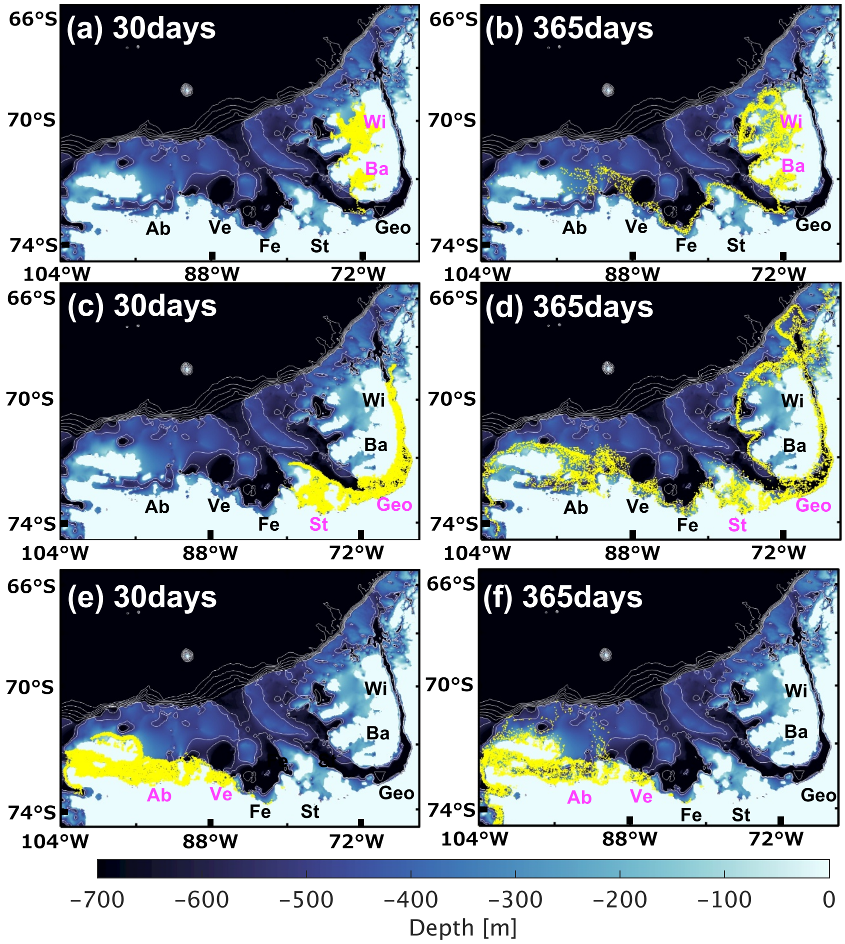

Figure 11. Spatial distributions of forwarding tracking particles (yellow points) released under the (a, b) Wilkins and Bach, (c, d) George VI and Stange, and (e, f) Venable and Abbot ice shelves in locations with mean basal melting and using time mean daily velocity (1992–2017). The days shown are relative to the start of the simulation (30 days: a, c, e; 365 days: b, d, f). The contours of depths of 500, 600, 1,000, 1,500, and 2,000 m are shown in white. The magenta words indicate the name of ice shelves where particles are released.

George VI, and Wilkins and Bach ice shelves, respectively (Table S5 in Supporting Information S1). The time taken for the particles to reach the AS is likely to be highly dependent on the location of the Ice Shelf. After 2 years of model integration, we found that ∼33% of particles released in the BS ice shelves are located in the AS.

3.5. Seasonal Variability of mCDW and AACC in the BS

To clearly illustrate the seasonal variability at key locations U to Z (see Figure 12 for the locations), we calculate the standard deviation of each monthly current speed at depths of 5 and 501m between 1992 and 2018. The standard deviation of each monthly current speed at a depth of 501 m reaches a maximum of ∼0.015 m s^{-1} in the Belgica Trough and Eltanin Basin (Figure 12a), coinciding with the mCDW pathways indicated by the red pathways P1, P2, and P3 in Figure 1. The current speed at 501 m along the coast (red P2 pathway in Figure 1) shows seasonal variability, with higher velocities in austral summer (e.g., locations W and X in Figures 12e and 12f), contrary to the current at 501 m close to shelf break (locations U and V in Figures 12c and 12d). At locations W and X, a clear seasonal variability with a maximum current speed in summer (January–March) and a minimum in winter (June–August) can be identified for 42% and 58% of the simulated years, respectively. However, at locations U and V, such a seasonal variability can only be identified for 31% and 27% of the simulated years, respectively.

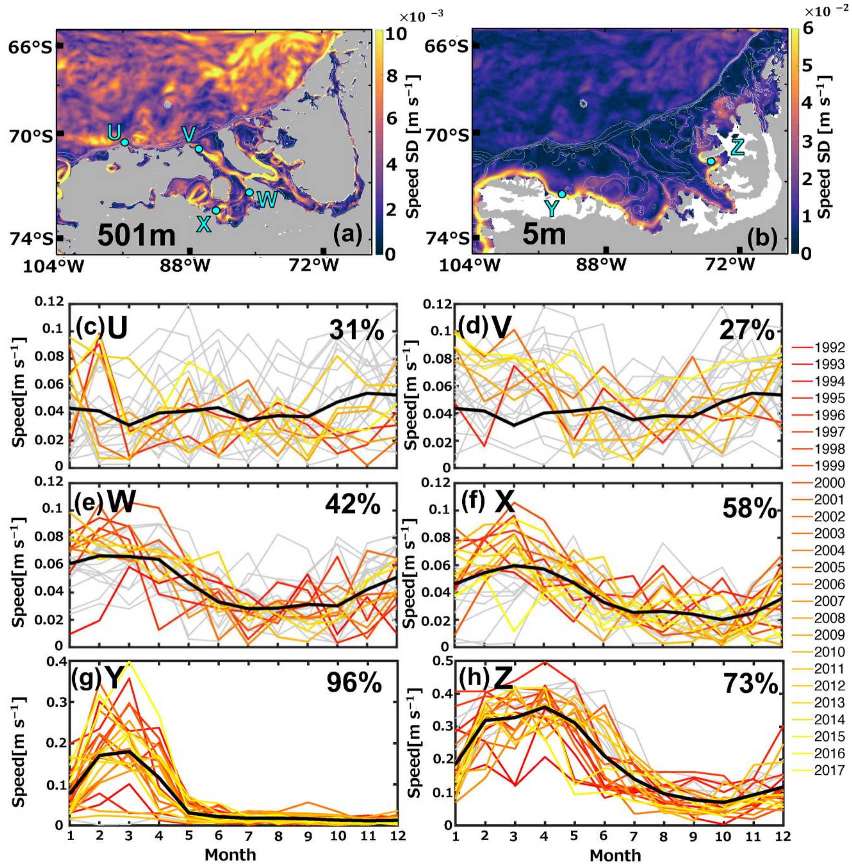

Figure 12. (a, b) The standard deviation of monthly ocean speed deduced between 1992 and 2017 at depths of (a) 501 m and (b) 5 m. The contours of depths of 500, 600, 1,000, 1,500, and 2,000 m are shown in white. Light blue circles (U–Z) indicate the locations shown in (c–h). (c–h) The time series of monthly speed between 1992 and 2017 at locations (c) U, (d) V, (e) W, (f) X at 501m depth, and (g) Y, (h) Z at 5 m depth. The colored lines indicate years with a maximum speed between January and March for (c–f) and between January and April for (g, h). Thick black lines show the monthly mean speed in all years. The value in the upper right shows the ratio of the number of warm-colored lines being compared to the total (26 years).

The standard deviation of each monthly velocity at a depth of 5 m reaches a maximum of ~0.06 m s^{-1} close to the coast (Figure 12b), overlapping with the AACC pathway (see Figure 2b, and blue pathways P7 and P8 in Figure 1). The time series of ocean speed at 5 m at locations *Y* and *Z* exhibits seasonal variability with higher velocities in summer (Figures 12g and 12h). At locations *Y* and *Z*, 96% and 73% of the total model simulated years exhibited a maximum current speed in summer (January–April) and a minimum in winter (June–August), respectively.

4. Discussions

4.1. Factors Controlling mCDW Intrusion Seasonality

The mCDW intrusions toward the Venable and Abbot ice shelves show seasonal variability with higher velocities in summer, only in the coastal area (see Figures 12e and 12f). However, the seasonal variability of mCDW intrusions (current velocities) tends to be weak near the coast (K. Assmann et al., 2019; Dotto et al., 2019; Dundas et al., 2022; Ha et al., 2014; T.-W. Kim et al., 2017; B. Webber et al., 2017). Additionally, our simulations show that the velocities along the pathway of mCDW in the Belgica Trough are seasonally variable only in the coastal region, whereas an analysis of mooring results reveals widespread and spatially coherent intra-seasonal structures for the Antarctic Peninsula, including the Marguerite Trough (McKee & Martinson, 2020a, 2020b). These structures are not confined to the coastal regions but also expand to the shelf-break regions and the continental slope. Here, we investigate the seasonally varying mCDW intrusions mechanism in the coastal areas of the

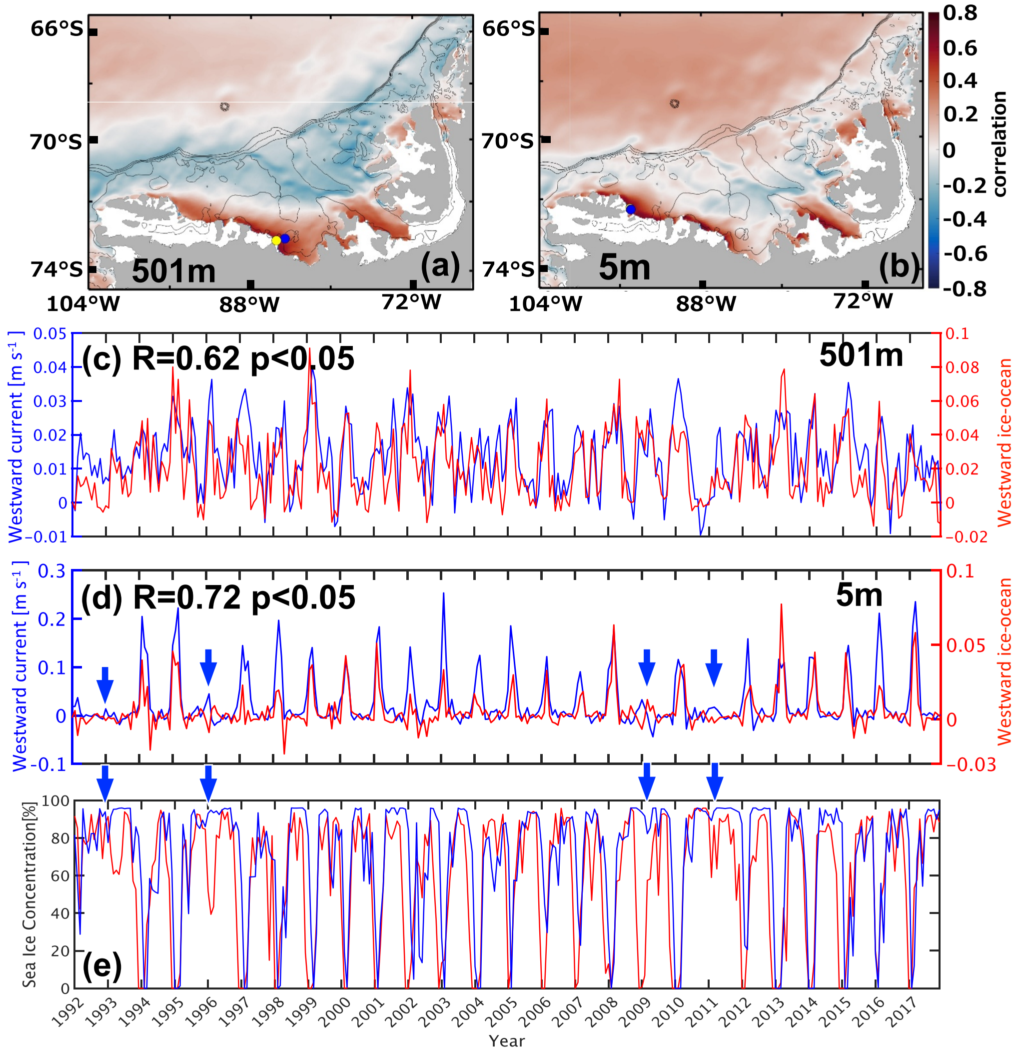

Figure 13. Correlations between westward ocean current at depths of (a) 501 m and (b) 5 m (blue dots) and the overall westward ice-ocean stress in the BS. The yellow dots indicate the locations of maximum correlation coefficients between the westward ocean current and westward ice-ocean stress. In (b), the yellow dot is hidden by the blue dot. (c, d) Time series of monthly ocean speed (blue) at depths of (c) 501m and (d) 5m and (red) westward ice-ocean stress at the maximum correlation coefficients from 1992 to 2017. (e) Time series of monthly sea-ice concentration at blue dots in (a) (red line) and (b) (blue line).

Eltanin Basin focusing on coastal trapped waves (CTWs) generated by the combination of lower sea-ice concentrations and wind stress blowing.

We calculate the correlation between westward current at a depth of 501 m and westward component of ice-ocean stress over the BS. We compute ice-ocean stress as the weighted combination of the wind stress over the ice-free ocean and the ice/ocean stress under the ice. The zero-lag correlation coefficients are relatively large in the coastal area (see Figure 13a, 0.63 at the highest correlation point). A comparison of ice-ocean stress and mCDW speed for the 1992–2017 period shows good agreement, with both peaking in the summer months of each year (see Figure 13c). Seasonal variabilities in mCDW speed are caused by the combination of lower sea-ice concentrations and wind stress blowing from the land to the coast of Antarctica, which enhances the direct westward ice-ocean stress on the ocean (Figure S6 in Supporting Information S1). Westward wind stress is strong throughout the year, but westward ice-ocean stress is weak when sea ice concentration is high in winter. This situation indicates that internal ice stresses prevent the free drift ice response to the wind stress in winter.

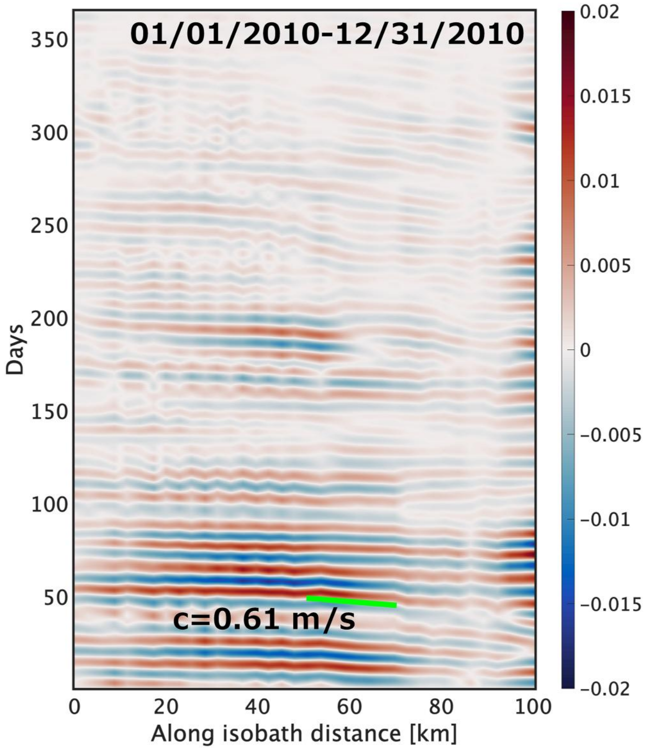

Figure 14. Hovmöller diagram of bandpass-filtered north-westward velocity [m s^{-1}] along the 850-m isobath (83.1°W–84.7°W) in the Belgica Trough: 10–15-day pass band. The *y*-axes are days from January 1 to December 31 in 2010. Green slanted line indicates inferred phase velocity.

In coastal areas, shoreward Ekman transport by westward wind causes the downwelling of seawater, which propagates westward as CTWs in various time scales (Gill & Clarke, 1974; Gill & Schumann, 1974; Nakayama et al., 2012). The propagation of CTWs is visible during the summer throughout the model-driven period. In 2010, shown as an example, the northwestward velocities within the Eltanin Basin are large from January to March compared with other seasons (Figure 14; Figure S7 in Supporting Information S1). The phase speed of the waves on the shelf, as derived from the slope of the lime-green lines, is roughly 0.61 m s^{-1} in the 10–15 days band. The amplitude is roughly 0.015 m s^{-1} until March and roughly 0.005 m s^{-1} after that. Therefore, we suggest that the warm water intrusions toward the Venable Ice Shelf along the Eltanin Basin show peaks of higher velocities in summer, likely caused by CTWs. The CTWs may be weaker in reality than reproduced by the model because simulated summer sea ice is under-represented in the Belgica Trough. The required condition for mCDW to speed up in response to the alongshore wind is a submarine glacial trough extending parallel to the coastline as the Eltanin Basin. Such topography is rare in West Antarctica and East Antarctica, suggesting that this feature may be unique to the BS.

4.2. Factors Controlling the Seasonality of AACC Strength

In Antarctica, the AACC is modulated by buoyancy injected by ice-shelf meltwater and wind stress (K. M. Assmann et al., 2005; Holland et al., 2010; Moffat et al., 2008; Núñez-Riboni & Fahrbach, 2009; D. A. Smith et al., 1999). In the western AS, the AACC has been identified as a strong westward current with a variable baroclinic component generated by easterly winds (C.-S. Kim et al., 2016). A coastal current is also found along the Western Antarctic Peninsula in ocean simulations, which is controlled by the prevailing easterly winds (Holland et al., 2010). For the BS, the mechanism generating and controlling of the AACC is proposed to be injection of glacial meltwater (Schubert et al., 2021). This study focuses on wind, which is known as the traditional AACC driving mechanism (C.-S. Kim et al., 2016; Núñez-Riboni & Fahrbach, 2009).

To clarify the seasonal variability of AACC velocity, we calculate its correlation with westward ice-ocean stress over the BS. The correlation coefficients are relatively large in the coastal area (see Figure 13b, 0.72 at the highest point). The higher correlation coefficients in the coastal area are most likely related to the wind stress blowing from the land to the coastal area of Antarctica. A comparison of westward ice-ocean wind stress and westward AACC velocity for 1992–2017 shows that both peak in the summer months of December–March of each year, which is consistent for most years (see Figure 13d). The seasonal variability in AACC velocity is likely caused by lower sea-ice concentration in summer, which enhances the direct westward wind stress on the ocean. For 1993, 1996, 2009, and 2011, we do not see clear peaks in the zonal wind stress and AACC speeds. This is likely caused by higher simulated sea-ice concentration in these years (see blue arrows in Figures 13d and 13e). When sea-ice concentration is higher and sea-ice movement is restricted in summer, wind stress over the sea ice cannot be transferred to the ocean. This can be confirmed as we find a significant negative correlation between AACC speed and sea ice concentration (Figure S8 in Supporting Information S1; −0.73 in the zero-lag correlation).

5. Conclusions

The Bellingshausen Sea is host to some rapidly thinning ice shelves, but the sparsity of in situ observations has limited our understanding of the ocean circulations over the continental shelves. We develop a regional ocean model using MITgcm and evaluate the model by comparing it with observations. Based on this simulation, we investigate drivers and pathways of mCDW intrusions as well as the spreading of glacial meltwater from the BS ice shelves.

Simulated cross-shelf mCDW intrusions occur mainly from the shelf break of the Belgica and Marguerite troughs. The heat transport through the Belgica Trough is ∼2.8 times larger than that through the Marguerite Trough (Figure 10). For the Belgica Trough, the simulated mCDW travels along the Belgica trough at the shelf break and separates into two pathways, toward the Eltanin Basin and the Latady Trough (P1, P2, and P3 red pathways in Figure 1). The mCDW intrusions toward the Eltanin Basin show clockwise circulation (P2 red pathway in Figure 1). The mCDW intrusions toward the Latady Trough again separate into two pathways (P4 and P5 red pathways in Figure 1) toward the shelf break and the Ronne Entrance near the southern George VI Ice Shelf (P3, P4, and P5 red pathways in Figure 1). From backward particle experiments, it takes ∼7.9 months for mCDW to get from the Belgica Trough shelf break to the southern George VI Ice Shelf (Figure 9 and Table S5 in Supporting Information S1). For the Marguerite Trough, the simulated mCDW intrudes at the shelf break and flows directly toward the northern George VI Ice Shelf through the submarine glacial trough (Figures 2 and 3). From the backward particle experiments, it takes ∼11.7 months for mCDW to get from the Marguerite Trough shelf break to the northern George VI Ice Shelf (Figure 9 and Table S5 in Supporting Information S1). These results indicate that the mCDW intrusions from the Belgica Trough have a significant impact on the melting of the BS ice shelves.

We conduct forward particle experiments to investigate the spreading of glacial meltwater from the BS ice shelves (Figure 11). The glacial meltwater is transported by a strong westward AACC above depths of 200 m (Figures 2 and 3) and mainly spreads westward into the AS within ∼7 months (Table S5 in Supporting Information S1). After 2 years of model integration, ∼33% of particles from the BS are transported into the AS. This result implies that glacial meltwater from the BS ice shelves may affect AS near surface water mass characteristics, supporting implications from observational studies (Ruan et al., 2021; Schubert et al., 2021).

The simulated mCDW shows seasonal variability with higher velocities in summer in the Eltanin Basin close to the Venable Ice Shelf (Figures 12a, 12e, and 12f). By calculating correlation coefficients between westward current at a depth of 501m and ocean westward component of ice-ocean stress over the BS, we show that the warm water intrusions toward the Venable Ice Shelf show peaks of higher velocities in summer, likely caused by coastal trapped waves (Figures 13a, 13c, and 14). Seasonal variabilities in AACC velocities are possibly caused by lower sea-ice concentrations in summer, which enhances the direct westward wind stress on the ocean. We do not typically observe significant seasonal variability in mCDW intrusions toward the West Antarctic ice shelves (e.g., Webber et al., 2017). The strong seasonality observed for mCDW intrusions toward the Venable Ice Shelf can possibly be a special case, as the submarine glacial trough (80°W–88°W) is parallel to the coastal line (Figure 1), allowing coastal trapped waves to develop, as driven by westward wind stress.

Despite the BS having the second highest ice mass loss in Antarctica, we still do not fully understand how BS ice-shelf melting is controlled and how it will change in the future. Thus, it is essential to develop ocean simulation, evaluate against existing observations, and further improve model-data agreement. This study is a step toward understanding the BS ocean circulation by integrating models and observations.

Data Availability Statement

The model code, input, and results are available at https://doi.org/10.5281/zenodo.6570222 (Hyogo, 2022). They are also available at https://ecco.jpl.nasa.gov/drive/files/ECCO2/LLC1080_REG_AMS/Hyogo_et_al_2022. Data from JR165 are archived at the British Oceanography Data Center (https://www.bodc.ac.uk/data/documents/cruise/8529/). The marine mammal data were collected and made freely available by the International MEOP Consortium and the national programs that contribute to it (http://www.meop.net). Argo float data collected and made freely available by the International Argo Program and the national programs that contribute to it (https://argo.ucsd.edu, https://www.ocean-ops.org). The Argo Program is part of the Global Ocean Observing System. Argo float data were downloaded together with other historical CTD data as part of the World Ocean Database 2018 (https://www.ncei.noaa.gov/products/world-ocean-database), a National Centers for Environmental Information standard product. The Bootstrap Sea Ice Concentrations from Nimbus-7 SMMR and DMSP SSM/I-SSMIS, Version 3 data are archived at the National Snow and Ice Data Center (NSIDC), a NASA Distributed Active Archive Center (https://nsidc.org/data/nsidc-0079/versions/3) (Comiso, 2017). Some of the figures are created with software MATLAB R2022a and Ocean Data View.

Acknowledgments
This study was supported by the Cooperative Research Activities of Collaborative Use of Computing Facility of the Atmosphere and Ocean Research Institute, the University of Tokyo. We thank Hong Zhang, Andrew Thompson, and Ayako Abe-Ouchi for their useful comments and suggestions. We also thank the officers, crew, and scientists on board JR165 (2007). SH was supported by JST, the establishment of university fellowships towards the creation of science technology innovation, Grant Number of JPMJFS2101. YN was supported by Grants-in-Aids for Scientific Research (21K13989) from the Ministry of Education, Culture, Sports, Science, and Technology in Japan, and by the Inoue Science Research Award from the Inoue Science Foundation. VM is supported by Grants-in-Aid for Scientific Research 22K1409402, 17H01157. Insightful comments from Laurence Padman and the one anonymous reviewers were very helpful for improvement of the manuscript. We also thank the 64th Japanese Antarctic Research Expedition, especially the overwintering team, for supporting Shuntaro Hyogo for over 1 year at Syowa Station.

References

Adusumilli, S., Fricker, H. A., Medley, B., Padman, L., & Siegfried, M. R. (2020). Interannual variations in meltwater input to the Southern Ocean from Antarctic ice shelves. *Nature Geoscience*, *13*(9), 616–620. https://doi.org/10.1038/s41561-020-0616-z

Antonov, J., Seidov, D., Boyer, T., Locarnini, R., Mishonov, A., Garcia, H., et al. (2010). In S. levitus (Ed.), *World Ocean Atlas 2009, vol. 2, salinity* (p. 184). U.S. Government Publishing Office.

Arndt, J. E., Schenke, H. W., Jakobsson, M., Nitsche, F. O., Buys, G., Goleby, B., et al. (2013). The International Bathymetric chart of the Southern Ocean (IBCSO) version 1.0—A new bathymetric compilation covering circum-antarctic waters. *Geophysical Research Letters*, *40*(12), 3111–3117. https://doi.org/10.1002/grl.50413

Assmann, K., Darelius, E., Wåhlin, A. K., Kim, T.-W., & Lee, S. H. (2019). Warm circumpolar deep water at the western getz ice shelf front, Antarctica. *Geophysical Research Letters*, *46*(2), 870–878. https://doi.org/10.1029/2018gl081354

Assmann, K. M., Hellmer, H. H., & Jacobs, S. S. (2005). Amundsen Sea ice production and transport. *Journal of Geophysical Research*, *110*(C12), C12013. https://doi.org/10.1029/2004jc002797

Bamber, J. L., Riva, R. E., Vermeersen, B. L., & LeBrocq, A. M. (2009). Reassessment of the potential sea-level rise from a collapse of the west Antarctic Ice Sheet. *Science*, *324*(5929), 901–903. https://doi.org/10.1126/science.1169335

Boyer, T. P., Baranova, O. K., Coleman, C., Garcia, H. E., Grodsky, A., Locarnini, R. A., et al. (2018). *NOAA atlas NESDIS 87* (pp. 1–207). World Ocean Database.

Castro-Morales, K., Cassar, N., Shoosmith, D. R., & Kaiser, J. (2013). Biological production in the Bellingshausen Sea from oxygen-to-argon ratios and oxygen triple isotopes. *Biogeosciences*, *10*(4), 2273–2291. https://doi.org/10.5194/bg-10-2273-2013

Comiso, J. C. (1986). Characteristics of Arctic Winter Sea ice from satellite multispectral microwave observations. *Journal of Geophysical Research*, *91*(C1), 975–994. https://doi.org/10.1029/jc091ic01p00975

Comiso, J. C. (2017). Bootstrap sea ice concentrations from Nimbus-7 SMMR and DMSP SSM/I-SSMIS, version 3 [Dataset]. *NASANationalSnow and Ice Data Center Distributed Active Archive Center*. Retrieved from https://nsidc.org/data/NSIDC-0079/versions/3

Cook, A. J., Holland, P., Meredith, M., Murray, T., Luckman, A., & Vaughan, D. G. (2016). Ocean forcing of glacier retreat in the western Antarctic Peninsula. *Science*, *353*(6296), 283–286. https://doi.org/10.1126/science.aae0017

Dawson, H. R., Morrison, A. K., England, M. H., & Tamsitt, V. (2023). Pathways and timescales of connectivity around the Antarctic continental shelf. *Journal of Geophysical Research: Oceans*, *128*(2), e2022JC018962. https://doi.org/10.1029/2022jc018962

Dee, D. P., Uppala, S. M., Simmons, A., Berrisford, P., Poli, P., Kobayashi, S., et al. (2011). The ERA-interim reanalysis: Configuration and performance of the data assimilation system. *Quarterly Journal of the Royal Meteorological Society*, *137*(656), 553–597. https://doi.org/10.1002/qj.828

Dinniman, M. S., Asay-Davis, X. S., Galton-Fenzi, B. K., Holland, P. R., Jenkins, A., & Timmermann, R. (2016). Modeling ice shelf/ocean interaction in Antarctica: A review. *Oceanography*, *29*(4), 144–153. https://doi.org/10.5670/oceanog.2016.106

Dinniman, M. S., & Klinck, J. M. (2004). A model study of circulation and cross-shelf exchange on the west Antarctic Peninsula continental shelf. *Deep Sea Research Part II: Topical Studies in Oceanography*, *51*(17–19), 2003–2022. https://doi.org/10.1016/j.dsr2.2004.07.030

Dinniman, M. S., Klinck, J. M., & Smith, W. O., Jr. (2011). A model study of circumpolar deep water on the West Antarctic Peninsula and Ross Sea continental shelves. *Deep Sea Research Part II: Topical Studies in Oceanography*, *58*(13–16), 1508–1523. https://doi.org/10.1016/j.dsr2.2010.11.013

Dotto, T. S., Garabato, A. C. N., Bacon, S., Holland, P. R., Kimura, S., Firing, Y. L., et al. (2019). Wind-driven processes controlling oceanic heat delivery to the Amundsen Sea, Antarctica. *Journal of Physical Oceanography*, *49*(11), 2829–2849. https://doi.org/10.1175/jpo-d-19-0064.1

Dundas, V., Darelius, E., Daae, K., Steiger, N., Nakayama, Y., & Kim, T.-W. (2022). Hydrography and circulation in the vicinity of the central Getz Ice Shelf: Two years of mooring observations. *Ocean Science Discussions*, 1–30.

Dutrieux, P., De Rydt, J., Jenkins, A., Holland, P. R., Ha, H. K., Lee, S. H., et al. (2014). Strong sensitivity of Pine Island ice-shelf melting to climatic variability. *Science*, *343*(6167), 174–178. https://doi.org/10.1126/science.1244341

Flexas, M. M., Thompson, A. F., Schodlok, M. P., Zhang, H., & Speer, K. (2022). Antarctic Peninsula warming triggers enhanced basal melt rates throughout west Antarctica. *Science Advances*, *8*(31), eabj9134. https://doi.org/10.1126/sciadv.abj9134

Forget, G., Campin, J.-M., Heimbach, P., Hill, C. N., Ponte, R. M., & Wunsch, C. (2015). ECCO version 4: An integrated framework for non-linear inverse modeling and global ocean state estimation. *Geoscientific Model Development*, *8*(10), 3071–3104. https://doi.org/10.5194/gmd-8-3071-2015

Fretwell, P., Pritchard, H. D., Vaughan, D. G., Bamber, J. L., Barrand, N. E., Bell, R., et al. (2013). Bedmap2: Improved ice bed, surface and thickness datasets for Antarctica. *The Cryosphere*, *7*(1), 375–393. https://doi.org/10.5194/tc-7-375-2013

Gill, A., & Clarke, A. (1974). Wind-induced upwelling, coastal currents and sea-level changes. In *Deep sea research and oceanographic abstracts* (Vol. 21, pp. 325–345).

Gill, A., & Schumann, E. (1974). The generation of long shelf waves by the wind. *Journal of Physical Oceanography*, *4*(1), 83–90. https://doi.org/10.1175/1520-0485(1974)004<0083:tgolsw>2.0.co;2

Graham, J. A., Dinniman, M. S., & Klinck, J. M. (2016). Impact of model resolution for on-shelf heat transport along the West Antarctic Peninsula. *Journal of Geophysical Research: Oceans*, *121*(10), 7880–7897. https://doi.org/10.1002/2016jc011875

Ha, H. K., Wåhlin, A., Kim, T., Lee, S., Lee, J., Lee, H., et al. (2014). Circulation and modification of warm deep water on the central Amundsen shelf. *Journal of Physical Oceanography*, *44*(5), 1493–1501. https://doi.org/10.1175/jpo-d-13-0240.1

Holland, P. R., Jenkins, A., & Holland, D. M. (2010). Ice and ocean processes in the Bellingshausen Sea, Antarctica. *Journal of Geophysical Research*, *115*(C5), C05020. https://doi.org/10.1029/2008jc005219

Hyogo, S. (2022). MITgcm model setup and output for "Modeling ocean circulation in the Bellingshausen Sea" [Dataset]. *Zenodo*. https://doi.org/10.5281/zenodo.6570222

Jacobs, S., Giulivi, C., & Mele, P. (2002). Freshening of the Ross Sea during the late 20th century. *Science*, *297*(5580), 386–389. https://doi.org/10.1126/science.1069574

Jacobs, S. S., Hellmer, H. H., & Jenkins, A. (1996). Antarctic ice sheet melting in the Southeast Pacific. *Geophysical Research Letters*, *23*(9), 957–960. https://doi.org/10.1029/96gl00723

Jenkins, A., & Jacobs, S. (2008). Circulation and melting beneath George VI ice shelf, Antarctica. *Journal of Geophysical Research*, *113*(C4), C04013. https://doi.org/10.1029/2007jc004449

Kalén, O., Assmann, K. M., Wåhlin, A. K., Ha, H. K., Kim, T. W., & Lee, S. H. (2016). Is the oceanic heat flux on the central Amundsen Sea shelf caused by barotropic or baroclinic currents? *Deep Sea Research Part II: Topical Studies in Oceanography*, *123*, 7–15. https://doi.org/10.1016/j.dsr2.2015.07.014

Kim, C.-S., Kim, T.-W., Cho, K.-H., Ha, H. K., Lee, S., Kim, H.-C., & Lee, J.-H. (2016). Variability of the Antarctic coastal current in the Amundsen Sea. Estuarine. *Coastal and Shelf Science*, *181*, 123–133. https://doi.org/10.1016/j.ecss.2016.08.004

Kim, T.-W., Ha, H. K., Wåhlin, A., Lee, S., Kim, C.-S., Lee, J. H., & Cho, Y.-K. (2017). Is Ekman pumping responsible for the seasonal variation of warm circumpolar deep water in the Amundsen Sea? *Continental Shelf Research*, *132*, 38–48. https://doi.org/10.1016/j.csr.2016.09.005

Kusahara, K., & Hasumi, H. (2014). Pathways of basal meltwater from Antarctic ice shelves: A model study. *Journal of Geophysical Research: Oceans*, *119*(9), 5690–5704. https://doi.org/10.1002/2014jc009915

Locarnini, R., Mishonov, A., Antonov, J., Boyer, T., Garcia, H., Baranova, O., et al. (2010). *World Ocean Atlas 2009, vol. 1: Temperature, chapter 2*. US Government Printing Office.

Losch, M. (2008). Modeling ice shelf cavities in a z coordinate ocean general circulation model. *Journal of Geophysical Research*, *113*(C8), C08043. https://doi.org/10.1029/2007JC004368

Losch, M., Menemenlis, D., Campin, J.-M., Heimbach, P., & Hill, C. (2010). On the formulation of sea-ice models. Part 1: Effects of different solver implementations and parameterizations. *Ocean Modelling*, *33*(1), 129–144. https://doi.org/10.1016/j.ocemod.2009.12.008

Marshall, J., Adcroft, A., Hill, C., Perelman, L., & Heisey, C. (1997). A finite-volume, incompressible navier Stokes model for studies of the ocean on parallel computers. *Journal of Geophysical Research*, *102*(C3), 5753–5766. https://doi.org/10.1029/96jc02775

Marshall, J., Hill, C., Perelman, L., & Adcroft, A. (1997). Hydrostatic, quasi-hydrostatic, and nonhydrostatic ocean modeling. *Journal of Geophysical Research*, *102*(C3), 5733–5752. https://doi.org/10.1029/96jc02776

Martinson, D., & McKee, D. (2012). Transport of warm upper circumpolar deep water onto the western Antarctic Peninsula continental shelf. *Ocean Science*, *8*(4), 433–442. https://doi.org/10.5194/os-8-433-2012

Martinson, D. G., Stammerjohn, S. E., Iannuzzi, R. A., Smith, R. C., & Vernet, M. (2008). Western Antarctic Peninsula physical oceanography and spatio–temporal variability. *Deep Sea Research Part II: Topical Studies in Oceanography*, *55*(18–19), 1964–1987. https://doi.org/10.1016/j.dsr2.2008.04.038

McKee, D. C., & Martinson, D. G. (2020a). Spatially coherent intraseasonal velocity fluctuations on the western Antarctic Peninsula shelf. *Journal of Geophysical Research: Oceans*, *125*(5), e2019JC015770. https://doi.org/10.1029/2019jc015770

McKee, D. C., & Martinson, D. G. (2020b). Wind-driven barotropic velocity dynamics on an Antarctic shelf. *Journal of Geophysical Research: Oceans*, *125*(5), e2019JC015771. https://doi.org/10.1029/2019jc015771

Moffat, C., Beardsley, R. C., Owens, B., & Van Lipzig, N. (2008). A first description of the Antarctic Peninsula Coastal Current. *Deep Sea Research Part II: Topical Studies in Oceanography*, *55*(3–4), 277–293. https://doi.org/10.1016/j.dsr2.2007.10.003

Nakayama, Y., Dimitris, M., Hong, Z., Michael, S., & Rignot, E. (2018). Origin of circumpolar deep water intruding onto the Amundsen and Bellingshausen Sea continental shelves. *Nature Communications*, *9*(3403), 3403. https://doi.org/10.1038/s41467-018-05813-1

Nakayama, Y., Menemenlis, D., Schodlok, M., & Rignot, E. (2017). Amundsen and Bellingshausen Seas simulation with optimized ocean, sea ice, and thermodynamic ice shelf model parameters. *Journal of Geophysical Research: Oceans*, *122*(8), 6180–6195. https://doi.org/10.1002/2016jc012538

Nakayama, Y., Ohshima, K. I., & Fukamachi, Y. (2012). Enhancement of sea ice drift due to the dynamical interaction between sea ice and a coastal ocean. *Journal of Physical Oceanography*, *42*(1), 179–192. https://doi.org/10.1175/jpo-d-11-018.1

Nakayama, Y., Schröder, M., & Hellmer, H. H. (2013). From circumpolar deep water to the glacial meltwater plume on the eastern Amundsen Shelf. *Deep Sea Research Part I: Oceanographic Research Papers*, *77*, 50–62. https://doi.org/10.1016/j.dsr.2013.04.001

Nakayama, Y., Timmermann, R., & H Hellmer, H. (2020). Impact of West Antarctic ice shelf melting on Southern Ocean hydrography. *The Cryosphere*, *14*(7), 2205–2216. https://doi.org/10.5194/tc-14-2205-2020

Nakayama, Y., Timmermann, R., Rodehacke, C. B., Schröder, M., & Hellmer, H. H. (2014). Modeling the spreading of glacial meltwater from the Amundsen and Bellingshausen Seas. *Geophysical Research Letters*, *41*(22), 7942–7949. https://doi.org/10.1002/2014gl061600

Núñez-Riboni, I., & Fahrbach, E. (2009). Seasonal variability of the Antarctic Coastal Current and its driving mechanisms in the Weddell Sea. *Deep Sea Research Part I: Oceanographic Research Papers*, *56*(11), 1927–1941. https://doi.org/10.1016/j.dsr.2009.06.005

Paolo, F. S., Fricker, H. A., & Padman, L. (2015). Volume loss from Antarctic ice shelves is accelerating. *Science*, *348*(6232), 327–331. https://doi.org/10.1126/science.aaa0940

Pritchard, H., Ligtenberg, S. R., Fricker, H. A., Vaughan, D. G., van den Broeke, M. R., & Padman, L. (2012). Antarctic ice-sheet loss driven by basal melting of ice shelves. *Nature*, *484*(7395), 502–505. https://doi.org/10.1038/nature10968

Regan, H. C., Holland, P. R., Meredith, M. P., & Pike, J. (2018). Sources, variability and fate of freshwater in the Bellingshausen Sea, Antarctica. *Deep Sea Research Part I: Oceanographic Research Papers*, *133*, 59–71. https://doi.org/10.1016/j.dsr.2018.01.005

Rignot, E., Jacobs, S., Mouginot, J., & Scheuchl, B. (2013). Ice-shelf melting around Antarctica. *Science*, *341*(6143), 266–270. https://doi.org/10.1126/science.1235798

Rignot, E., Mouginot, J., Scheuchl, B., Van Den Broeke, M., Van Wessem, M. J., & Morlighem, M. (2019). Four decades of Antarctic Ice Sheet mass balance from 1979–2017. *Proceedings of the National Academy of Sciences of the United States of America*, *116*(4), 1095–1103. https://doi.org/10.1073/pnas.1812883116

Rintoul, S. R. (2007). Rapid freshening of Antarctic bottom water formed in the Indian and Pacific oceans. *Geophysical Research Letters*, *34*(6), L06606. https://doi.org/10.1029/2006gl028550

Roquet, F., Charrassin, J.-B., Marchand, S., Boehme, L., Fedak, M., Reverdin, G., & Guinet, C. (2011). Delayed-mode calibration of hydrographic data obtained from animal-borne satellite relay data loggers. *Journal of Atmospheric and Oceanic Technology*, *28*(6), 787–801. https://doi.org/10.1175/2010jtecho801.1

Ruan, X., Speer, K. G., Thompson, A. F., Schulze Chretien, L. M., & Shoosmith, D. R. (2021). Ice-shelf meltwater overturning in the Bellingshausen Sea. *Journal of Geophysical Research: Oceans*, *126*(5), e2020JC016957. https://doi.org/10.1029/2020jc016957

Schauer, U., & Beszczynska-Möller, A. (2009). Problems with estimation and interpretation of oceanic heat transport–conceptual remarks for the case of Fram Strait in the Arctic Ocean. *Ocean Science*, *5*(4), 487–494. https://doi.org/10.5194/os-5-487-2009

Schubert, R., Thompson, A. F., Speer, K., Schulze Chretien, L., & Bebieva, Y. (2021). The Antarctic Coastal Current in the Bellingshausen Sea. *The Cryosphere Discussions*, *1–33*.

Schulze Chretien, L., Thompson, A., Flexas, M., Speer, K., Swaim, N., Oelerich, R., et al. (2021). The shelf circulation of the Bellingshausen Sea. *Journal of Geophysical Research: Oceans*, *126*(5), e2020JC016871. https://doi.org/10.1029/2020jc016871

Sheehan, P. M., Heywood, K. J., Thompson, A. F., Flexas, M. M., & Schodlok, M. P. (2023). Sources and pathways of glacial meltwater in the Bellingshausen Sea, Antarctica. *Geophysical Research Letters*, *50*(14), e2023GL102785. https://doi.org/10.1029/2023gl102785

Smith, B., Fricker, H. A., Gardner, A. S., Medley, B., Nilsson, J., Paolo, F. S., et al. (2020). Pervasive ice sheet mass loss reflects competing ocean and atmosphere processes. *Science*, *368*(6496), 1239–1242. https://doi.org/10.1126/science.aaz5845

Smith, D. A., Hofmann, E. E., Klinck, J. M., & Lascara, C. M. (1999). Hydrography and circulation of the west Antarctic Peninsula continental shelf. *Deep Sea Research Part I: Oceanographic Research Papers*, *46*(6), 925–949. https://doi.org/10.1016/s0967-0637(98)00103-4

St-Laurent, P., Klinck, J. M., & Dinniman, M. S. (2013). On the role of coastal troughs in the circulation of warm Circumpolar Deep Water on Antarctic shelves. *Journal of Physical Oceanography*, *43*(1), 51–64. https://doi.org/10.1175/jpo-d-11-0237.1

Talbot, M. (1988). Oceanic environment of George VI ice shelf, Antarctic Peninsula. *Annals of Glaciology*, *11*, 161–164. https://doi.org/10.3189/s0260305500006480

Thompson, A. F., Speer, K. G., & Schulze Chretien, L. M. (2020). Genesis of the Antarctic slope current in West Antarctica. *Geophysical Research Letters*, *47*(16), e2020GL087802. https://doi.org/10.1029/2020gl087802

Treasure, A. M., Roquet, F., Ansorge, I. J., Bester, M. N., Boehme, L., Bornemann, H., et al. (2017). Marine mammals exploring the Oceans pole to pole: A review of the MEOP consortium. *Oceanography*, *30*(2), 132–138. https://doi.org/10.5670/oceanog.2017.234

Wåhlin, A., Kalén, O., Arneborg, L., Björk, G., Carvajal, G., Ha, H. K., et al. (2013). Variability of warm deep water inflow in a submarine trough on the Amundsen Sea shelf. *Journal of Physical Oceanography*, *43*(10), 2054–2070. https://doi.org/10.1175/jpo-d-12-0157.1

Walker, C., & Gardner, A. S. (2017). Rapid drawdown of Antarctica's Wordie ice shelf glaciers in response to ENSO/Southern Annular Mode-driven warming in the Southern Ocean. *Earth and Planetary Science Letters*, *476*, 100–110. https://doi.org/10.1016/j.epsl.2017.08.005

Walker, D. P., Brandon, M. A., Jenkins, A., Allen, J. T., Dowdeswell, J. A., & Evans, J. (2007). Oceanic heat transport onto the Amundsen Sea shelf through a submarine glacial trough. *Geophysical Research Letters*, *34*(2), L02602. https://doi.org/10.1029/2006GL028154

Webber, B., Haywood, K., Stevens, D., Dutrieux, P., Abrahamsen, E., Jenkins, A., et al. (2017). Mechanisms driving variability in the ocean forcing of Pine Island Glacier. *Nature Communications*, *8*(1), 14507. https://doi.org/10.1038/ncomms14507

Webber, B. G., Heywood, K. J., Stevens, D. P., & Assmann, K. M. (2019). The impact of overturning and horizontal circulation in pine island trough on ice shelf melt in the eastern Amundsen Sea. *Journal of Physical Oceanography*, *49*(1), 63–83. https://doi.org/10.1175/jpo-d-17-0213.1

Wouters, B., Martin-Español, A., Helm, V., Flament, T., van Wessem, J. M., Ligtenberg, S. R., et al. (2015). Dynamic thinning of glaciers on the southern Antarctic Peninsula. *Science*, *348*(6237), 899–903. https://doi.org/10.1126/science.aaa5727

Wunsch, C., & Heimbach, P. (2013). Ocean circulation and climate-a 21st century perspective: Chapter 21–dynamically and kinematically consistent global ocean circulation and ice state estimates. *International Geophysics*, *103*, 553–579.

Zhang, H., Menemenlis, D., & Fenty, I. (2018). ECCO LLC270 ocean-ice state estimate.

Zhang, X., Thompson, A. F., Flexas, M. M., Roquet, F., & Bornemann, H. (2016). Circulation and meltwater distribution in the Bellingshausen Sea: From shelf break to coast. *Geophysical Research Letters*, *43*(12), 6402–6409. https://doi.org/10.1002/2016gl068998